



Response function generation for Cerenkov radiation production and transport in a TRIGA coolant channel

Jason A. Hearne^{*}, Pavel V. Tsvetkov

Texas A&M University, United States

ARTICLE INFO

Article history:

Received 29 July 2019

Received in revised form 31 October 2019

Accepted 5 November 2019

Available online 21 November 2019

Keywords:

Response function
Cerenkov radiation
TRIGA
MCNP

ABSTRACT

This study produces a response function that correlates the electron flux within a coolant channel in a TRIGA reactor to the amount of observable, visible Cerenkov light above the core. This response function is to be used in a study on using Cerenkov detection for spatial power profiling in a reactor. 23 electron energy bins and 16 spatial bins are used to create a matrix of 368 correlation factors that comprises the response function. It was tested to verify self-consistency by accounting for 92% of the Cerenkov photons 2 m above the core. The strength of the coupling between the Cerenkov above a coolant channel and the fission density in the core was also analyzed and it was found that in an 8×8 fuel pin lattice, 60.5% of the Cerenkov above a channel comes from gammas produced within the four surrounding pins and 88.1% comes from the closest 16 pins.

© 2019 Elsevier Ltd. All rights reserved.

1. Introduction

As part of a study on the use of Cerenkov radiation measurement as a spatial power profiling tool (Hearne, 2020), it became necessary to generate response function to relate the detectable Cerenkov light at a remote location to the electron flux at another location. Specifically, MCNP 6.1.1 Beta (Goorley, 2014) is used to correlate the energy dependent electron flux at locations within a coolant channel to the visible Cerenkov flux at a distance above the core. The advantage of using this response function is that it allows for the Cerenkov light above the core in a full-core model to be calculated without having to model computationally expensive Cerenkov production and visible light transport.

2. Fundamental physics of Cerenkov radiation

The system considered here involves measuring Cerenkov radiation, so a brief summary of the physics involved is included. Cerenkov radiation occurs when a charged particle passes through a dielectric medium at a velocity greater than the phase velocity of light in that medium. The phase velocity of light in a medium is the speed of light, c , divided by the frequency dependent refractive index in the medium as seen in Eq. (1), where $n(\omega)$ is the index of refraction for the medium for light with a frequency of ω and c is

the speed of light in a vacuum. The frequency dependent phase velocity is thus given by

$$c_{\text{phase}}(\omega) = \frac{c}{n(\omega)}. \quad (1)$$

The frequency (ω), energy (E) and wavelength (λ) of a photon are related by the Planck-Einstein relation, shown in Eq. (2):

$$E = \frac{hc}{\lambda} = h\omega, \quad (2)$$

where h is Planck's constant. Quantities may be referred to as dependent upon the energy, wavelength or frequency of a photon.

Cerenkov radiation is emitted in a cone travelling outwards and in the direction of the particle, similar to the effect of a sonic boom produced by an object exceeding the speed of sound in air or some other sound propagating medium. The single wavelength wave front produced by a particle is shown by the blue arrows in Fig. 1 (Horvath, 2006), where β is the ratio of the particle's velocity to the speed of light, and θ is given by Eq. (3):

$$\theta(\lambda) = \cos\left(\frac{1}{n(\omega)\beta}\right). \quad (3)$$

In a real system, there is a diffraction effect where different wavelengths of light are emitted at different angles from the particle's path based upon their indices of refraction. The intensity of photons emitted in a wavelength is expressed as the energy emit-

^{*} Corresponding author.

E-mail address: jasonhearn@tamu.edu (J.A. Hearne).

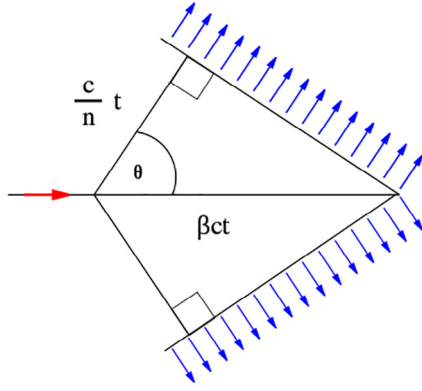


Fig. 1. Diagram of Cerenkov production directions, with Cerenkov photons shown in blue. (For interpretation of the references to colour in this figure legend, the reader is referred to the web version of this article.)

ted at a wavelength per unit path length traveled by the particle in the Frank-Tamm formula, given that β is greater than $1/n(\omega)$. The Frank-Tamm formula can be seen in Eq. (4):

$$\frac{d^2 E}{dx d\omega} = \frac{q^2}{4\pi} \mu(\omega) \omega \left(1 - \frac{1}{\beta^2 n^2(\omega)} \right). \quad (4)$$

The emission rate is approximately proportional to the frequency, causing the intensity to peak in the upper blue and ultraviolet ranges for Cerenkov radiation produced in water, resulting in the distinctive blue glow that can be seen in operating reactors or beta emitting sources kept under water. Further into and beyond the ultraviolet range, the frequency dependent index of refraction of water drops below 1, preventing the production of Cerenkov photons with higher frequencies.

The constraint that β must be greater than $1/n$ also provides a lower limit for the velocity and energy of charged particles. Using an approximated constant n of 1.33 for water, the minimum value of β for Cerenkov production is 0.75, which in the case of electrons corresponds to an energy of 261 keV, meaning that electrons with energies below 261 keV will not produce Cerenkov radiation in water, and when an electron's energy drops below 261 keV, it stops giving off Cerenkov photons. However, slightly lower energy photons can still produce some Cerenkov radiation in water at shorter wavelengths, such as those in the near UV range, because the frequency dependent index of refraction goes up to a peak value of 1.44, corresponding to a minimum value of β of 0.694, setting the cutoff electron energy at this limiting wavelength to 200 keV. So the true electron energy cutoff for Cerenkov production in water is 200 keV. This means that electrons with energies below 200 keV do not need to be transported in the models as they will not produce any further Cerenkov photons.

The visible photons produced by Cerenkov radiation are transported through water with little attenuation. The 1-dimensional attenuation of light in a medium is given by Eq. (5) for photons of a given wavelength and the corresponding energy:

$$I(\lambda) = I_0(\lambda) * e^{-\alpha(\lambda)r}, \quad (5)$$

where I is the intensity at a point, I_0 is the intensity at the source and r is the distance from the source, and α is the absorption or attenuation coefficient of the medium. For a point source, the intensity is also divided by $4\pi r^2$ to account for geometrical attenuation.

As indicated in Eq. (5), the attenuation coefficient in a medium, $\alpha(\lambda)$, is a function of the wavelength. In pure water, the attenuation coefficient is 1.26 m^{-1} in the far UV range at a wavelength 190 nm and falls to 0.0100 m^{-1} at a wavelength of 320 nm, near the transition to visible light (Quickenden and Irving, 1980). In the visible spectrum, the absorption coefficient in water remains in the

0.01 m^{-1} to 0.02 m^{-1} range for wavelengths up to 550 nm, corresponding to green light, beyond which it increases to 0.2 m^{-1} at around 700 nm wavelength, corresponding to red light (Litjens et al., 1999). The low, nearly constant attenuation coefficient in the range between 320 nm and 550 nm is important because this contains the portion of the visible spectrum in which most Cerenkov photons are emitted. With the average detection distance of approximately 2 m and the maximum attenuation coefficient of 0.02 m^{-1} for the photons of interest, the portion of the remaining intensity is $e^{-0.4}$, or 0.9608. This represents a maximum loss of 4% of the photons of interest through attenuation, so it has been deemed unnecessary to account for losses to attenuation beyond what is done automatically in the models.

3. Mathematical formulation of Cerenkov transport

The Cerenkov light above the core is caused by the Cerenkov production within a channel, which is directly proportional to the electron flux in the channel. The electron flux within a coolant channel is proportional to the gamma flux within the channel, because gammas produce the electrons and the range of electrons in water is small for most of the energy range of electrons present in the coolant. The lowest energy Cerenkov producing electrons with 200 keV have a range in water of $4.5 \times 10^{-2} \text{ cm}$; 1 MeV electrons have a range of 0.44 cm and 2 MeV electrons have a range of 0.98 cm (Berger et al., 2017). A plot showing values for the electron flux per unit energy in the coolant next to the Continuous Slowing Down Approximation (CSDA) range of the electrons can be seen in Fig. 2. The range for most of the electrons present in the coolant is less than 1 cm, so the electron flux in the middle of the coolant channel is almost entirely due to free electrons produced within the channel.

In an operating TRIGA reactor, the gamma flux in a coolant channel is primarily caused by the fissions in the surrounding fuel pins, more so than for a normal power reactor, because the TRIGA is not operated constantly, so the buildup of fission products is less. If the reactor is at zero or very low power, the Cerenkov flux will no longer be proportional to reactor power, as the gammas produced by fission products become a significant contribution to the total gamma flux. The fission rate density in fuel is proportional to the neutron flux as seen in Eq. (6):

$$\text{Fission density} = \Phi_{\text{neutron}} \Sigma_{\text{fission}}. \quad (6)$$

Thus, the Cerenkov observed above a channel is an indication of the power density and neutron flux within the surrounding pins. A diagram showing the progression from neutron flux to Cerenkov detection is shown in Fig. 2. The only step that involves spatial transport over a distance greater than a few cm is the transport of the Cerenkov photons through the coolant, which occurs in a straight line due to the wave nature of low energy light; every other step occurs close to the fuel rod or at the detector. There is some spatial blurring caused by the distance travelled by the gammas from the fuel pin to the coolant channels, but most gammas do not travel more than a pin pitch away, due to attenuation. The degree to which gammas from a pin propagate to distant coolant channels is analyzed in a later section.

The production and transport of light can be modeled by the general steady state photon transport equation can be seen in Eq. (7) (Wang and Wu, 2007):

$$\begin{aligned} \mathbf{s} \cdot \nabla \Psi_{\text{photon}}(\mathbf{r}, \mathbf{s}, E) = & -\mu_t \Psi_{\text{photon}}(\mathbf{r}, \mathbf{s}, E) \\ & + \mu_s \int_0^\infty dE' \int_{4\pi} d\mathbf{s}' \Psi_{\text{photon}}(\mathbf{r}, \mathbf{s}', E') P(\mathbf{s}', \mathbf{s}, E, E) + S(\mathbf{r}, \mathbf{s}, E), \end{aligned} \quad (7)$$

where \mathbf{r} is the position vector in space, \mathbf{s} is the unit direction vector, $\Psi_{\text{photon}}(\mathbf{r}, \mathbf{s}, E)$ is the photon flux at point \mathbf{r} in direction \mathbf{s} with energy

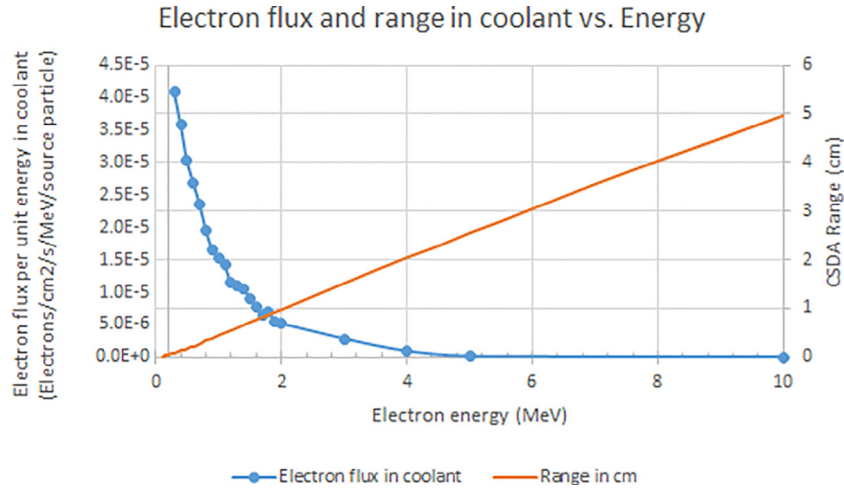


Fig. 2. Electron flux within a coolant channel and CSDA range of electrons in water vs. electron energy.

E , $\mu_t(E)$ is the energy dependent attenuation coefficient (similar to the total macroscopic cross section), μ_s is the scattering coefficient, $P(\mathbf{s}', \mathbf{s}, E', E)$ is the probability of a photon with direction \mathbf{s}' and energy E' scattering into the direction \mathbf{s} and energy E . The last term, $S(\mathbf{r}, \mathbf{s}, E)$ is the spatial, angle and energy dependent photon source term. The medium in which the photons are propagating and being produced is assumed to be homogenous.

For Cerenkov photons, the source term $S(\mathbf{r}, \mathbf{s}, E)$ can be approximated by Eq. (8):

$$S(\mathbf{r}, \mathbf{s}, E) = \frac{1}{4\pi} \int dE' \Phi_{\text{Electron}}(\mathbf{r}, E_e') \Sigma_{\text{Cerenkov}}(E_e', E), \quad (8)$$

where $\Phi_{\text{Electron}}(\mathbf{r}, E_e')$ is the spatial and energy dependent scalar electron flux. The quantity $\Sigma_{\text{Cerenkov}}(E_e', E)$ is the energy dependent macroscopic cross section for Cerenkov production by electrons, equal to the number of Cerenkov photons of energy E produced by an electron of energy E_e' per unit path length. This approximation adds the assumption that the electron flux is isotropic.

To find the Cerenkov flux at a specific point \mathbf{r} with photons within an angle range $d\mathbf{s}$ of a specified direction \mathbf{s} , a solution to some form of Eq. (5) must be obtained. This flux only depends on photons produced or scattered in the region contained by the a cone of angle $d\mathbf{s}$ opening away from the point \mathbf{r} in the direction $-\mathbf{s}$. Viewing a coolant channel from a significant distance above the core provides a very small angle view of a thin, constant width region that produces Cerenkov photons. In such a situation where the angle range $d\mathbf{s}$ is small and the cross sectional area of the region contributing to the flux is both small and constant, this can be approximated by a line integral starting at \mathbf{r} in the direction of $-\mathbf{s}$. This is an integral form of a solution of Eq. (5) and can be seen in Eq. (9):

$$\Psi_{\text{photon}}(\mathbf{r}, \mathbf{s}, E) = \int_0^\infty dr' \frac{e^{-\mu_t(E)r'}}{r'^2} * \left[\left\{ \int_E^\infty dE' \int_{4\pi} d\mathbf{s}' \Psi_{\text{photon}}(\mathbf{r} - \mathbf{r}'\mathbf{s}, \mathbf{s}') P(\mathbf{s}', \mathbf{s}, E', E) \right\} + S(\mathbf{r} - \mathbf{r}'\mathbf{s}, \mathbf{s}, E) \right]. \quad (9)$$

The variable r' represents the distance from the point \mathbf{r} . The $\exp(-\mu_t(E)r')$ term accounts for attenuation, while the $1/r'^2$ term is for the dissipation over distance from a point source. This accounts for the production of photons moving in the direction of interest, and the scattering of photons into that direction along the line tracing backwards along the vector.

The Cerenkov photons being detected have wavelengths in or very near the visible range, where light behaves less like a particle. The scattering coefficient of visible photons in pure water ranges from 10^{-1} m^{-1} for 350 nm photons to 10^{-3} m^{-1} for 600 nm photons (Morel, 1974). This means the mean free path for scattering is greater than 10 m, so the effect of scattering is expected to be very small. Therefore, an approximation can be made such that the scattering of visible photons into the angle and energy range is neglected as a source of photons contributing to the flux, and is only accounted for as part of the attenuation term, μ_t . This allows the scattering term, $P(\mathbf{s}', \mathbf{s}, E', E)$, and its corresponding integrals over angle and energy from Eq. (7) to be dropped. This leaves only the source term, the attenuation and the $1/r'^2$ dependence. This approximation simplifies Eq. (9) to create Eq. (10):

$$\Psi_{\text{photon}}(\mathbf{r}, \mathbf{s}, E) = \int_0^\infty S(\mathbf{r} - \mathbf{r}'\mathbf{s}, \mathbf{s}, E) \frac{e^{-\mu_t(E)r'}}{r'^2} dr'. \quad (10)$$

Using Eq. (6) for the source term in Eq. (10) gives the Cerenkov flux at a location as a function of the electron flux as seen in Eq. (11):

$$\Psi_{\text{photon}}(\mathbf{r}, \mathbf{s}, E) = \int_0^\infty dr' \frac{1}{4\pi} \int dE' \Phi_{\text{Electron}}(\mathbf{r} - \mathbf{r}'\mathbf{s}, E') \Sigma_{\text{Cerenkov}}(E', E) \frac{e^{-\mu_t(E)r'}}{r'^2}. \quad (11)$$

This infinite line integral can be approximated using a discretization that slices the region where significant contributions to the Cerenkov flux are made into segments. The spatial discretization accounts for spatial variations in the electron flux between bins, but not within the bins, so it is accurate as long as the variation within a bin is small. The contribution from Cerenkov photons produced outside of the discretization region is not counted, so the region should be large enough that the production of Cerenkov outside of it is small compared to the total production within the spatial bins. The energy integral can be approximated using another discretization that separates the energy dependent electron flux into bins. As long as the electron flux bins contain the entire energy range of the Cerenkov producing electrons, the only error introduced is in the averaging of the effects of the electron flux within a bin. This error depends on how much the electron flux and energy dependent Cerenkov production cross section vary within each energy bin. If small enough energy and spatial bins are used, the total error introduced by discretization is small. Applying both discretizations to Eq. (11) yields Eq. (12):

$$\Psi_{\text{photon}}(\mathbf{r}, \mathbf{s}, E) = \frac{1}{4\pi} \sum_{n=1}^{E_{\text{bins}}} \sum_{m=1}^{\text{Segments}} \Phi_{\text{Electron}}(z_m, E_n) \Sigma_{\text{Cerenkov}}(E_n, E) \frac{e^{-\mu_t(E) \cdot r_m}}{r_m^2}. \quad (12)$$

The total flux of visible light can be obtained from $\Psi_{\text{photon}}(\mathbf{r}, \mathbf{s}, E)$ if the energy dependence is removed by integrating over the photon energy range corresponding to visible light. This gives a total visible photon flux shown in Eq. (13):

$$\Psi_{\text{Visible}}(\mathbf{r}, \mathbf{s}) = \int_{1.77\text{eV}}^{3.17\text{eV}} dE \Psi_{\text{photon}}(\mathbf{r}, \mathbf{s}, E) \quad (13)$$

A final simplification can be made that combines the $1/4\pi$, the Cerenkov production term, the exponential attenuation and the $1/r^2$ term into a single spatial and electron energy dependent Cerenkov response function. This response function is a correlation between the electron flux in a bin and the amount of Cerenkov light that reaches the detection point. It is comprised of a set of correlation factors for each combination of m and n . One correlation factor, the value of the response function $\Sigma_{\text{Response}}(z_m, E_n)$ for location m and electron energy bin n is given by Eq. (14):

$$\Sigma_{\text{Response}}(z_m, E_n) = \int_{1.77\text{eV}}^{3.17\text{eV}} dE \Sigma_{\text{Cerenkov}}(E_n, E) \frac{e^{-\mu_t(E) \cdot r_m}}{r_m^2}. \quad (14)$$

The response function's behavior is similar to an electron cross section, because it is the amount of visible Cerenkov light detected at the detection point per unit of electron path length in the coolant channel. This allows Eq. (12) to be rewritten as Eq. (15):

$$\Psi_{\text{Visible}}(\mathbf{r}, \mathbf{s}) = \sum_{n=1}^{E_{\text{bins}}} \sum_{m=1}^{\text{Segments}} \Phi_{\text{Electron}}(z_m, E_n) \Sigma_{\text{Response}}(z_m, E_n). \quad (15)$$

If the response function is known, the only thing required to obtain the visible photon flux above the core is the spatial and energy dependent electron flux within the coolant channels.

The determination and verification of the response cross sections is done using MCNP and covered in the Electron to Cerenkov flux correlation section. Eq. (11) and the correlation factors can then be used to determine the amount of Cerenkov detected above the core without requiring the computationally expensive simulation of Cerenkov photons in the whole core. It also avoids issues with visible photons sometimes not transporting correctly through lattices or opaque materials in MCNP 6.1.1. The application of this approach has been implemented at the full core level in (Hearne, 2020).

4. Electron to Cerenkov flux response function generation

The discretized values of the response function, $\Sigma_{\text{Response}}(z_m, E_n)$, from Eqs. (14) and (15) forms a set of correlation factors. The correlation relates the electron flux within a space with an energy within a specific range to the resulting visible Cerenkov flux at a distant point. MCNP 6.1.1 Beta was used to model Cerenkov transport and to produce the correlation factors that form the response function. MCNP 6.1.1 Beta has added the capability to track photons down to 1 eV of energy (in the infrared range), to account for refraction in materials and to produce and transport Cerenkov radiation. This feature has been verified by Los Alamos National Lab to produce Cerenkov photons in a way that is consistent with other modeling software (Durkee and James, 2013). The index of refraction of a material is added in the material card, using either refi, refc or refs for a constant, Cauchy or Sellmeier treatment of refraction (Goorley, 2014). When Cerenkov photons are being produced in this research effort, the Sellmeier treatment is used. The Sellmeier treatment of refraction has greater agreement with measurements over a wider range of wavelengths than the simplified

Cauchy equation or the constant approximation. Using the Sellmeier treatment, the Cerenkov production is governed by a discretized form of the Frank Tamm formula shown in Eq. (16):

$$N = 2\pi\alpha L^2 \sum_{i=1}^l \left(\frac{1}{\lambda_i} - \frac{1}{\lambda_{i-1}} \right) \left(1 - \frac{1}{\beta_i^2 n_i^2} \right). \quad (16)$$

Here N is the number of photons emitted, α is the fine structure constant, L is the total path length, λ is the wavelength, β is the ratio of the charged particle's speed to the speed of light and n is the frequency dependent index of refraction. The Sellmeier coefficients are implemented in the model with an addition to the material card for water of "refs = 0.56840 5.1018e-3 1.7262e-1 1.8211e-2 2.0862e-2 2.6207e-2". Transporting visible photons through materials that do not have a refractive index specified was found to be inaccurate so it is not done in this study.

A correlation factor is generated for each 23 electron energy bins ranging from 200 keV to 10 MeV and 16 spatial bins. To determine these correlation factors, a simplified MCNP model of a single coolant channel within the TRIGA reactor is used. The spatial region considered for the tally is a 1 cm radius cylinder in the coolant channel, nearly touching the 4 neighboring pins. This region in relation to the surrounding pins can be seen in Fig. 5.

The cylindrical region between the pins is segmented into 16 spatial bins along the vertical (z) axis, each 4 cm long, ranging from $z = -32$ cm to $z = 32$ cm below and above the core midplane. This produces a total of $16 \times 23 = 368$ spatial and energy bins for which a correlation is found. The Cerenkov flux is tallied at a location 200 cm above the core midplane and only counts photons with energies between 1.76 eV and 3.17 eV, corresponding to visible light. In Fig. 5, a diagonal cross section of the 4 pin model can be seen, showing two of the pins and the coolant channel. As an example, one segment is singled out in the right side of the figure.

Due to the large number of correlations that must be obtained, a very simple model is run with only photons and electrons to obtain reasonably precise correlation factors. This model consists of a tube of water representing a coolant channel and the region above it. The column of water is surrounded by regions of zero photon importance in which photons are killed. The zero importance region must be made of water in the model instead of the customary vacuum to prevent the occurrence of total internal reflection effects caused by differing indices of refraction. The white regions of the right side of Fig. 5 are zero photon importance in this model. The electron importance is set to zero everywhere except for in the spatial region that the correlation is being calculated for, and the electron physics card is set to kill all electrons with energies below the lower energy bound of the bin for which the correlation factor is being determined. In Fig. 5, the red region would be the only region with a nonzero electron importance for a run producing a correlation factor for that segment. Then, the source definition card is set to homogeneously spawn electrons in the region of interest with an initial energy distribution that approximately results in a flat energy profile within the energy bin range. The electron flux is tallied with much smaller energy sub-bins to ensure that only electrons within the energy bin are present and that there is a close to flat energy profile within the correlation factor bin. If it is found that the electron energy profile within the range is not flat, the initial electron energy distribution on the SDEF card is adjusted and the run is repeated until a satisfactorily flat profile is obtained. The initial electron energy distribution to create a close to flat energy profile within the cell had a linear increase with energy; a uniform initial energy distribution would not create a flat energy profile, as the high energy electrons would slow down and thus increase the flux in the lower energy portion of the bin.

The Cerenkov production option added in MCNP6.1.1 Beta is turned on for these models and the photon energy cutoff is reduced

to the minimum allowable value of 1 eV. The electrons in the water thus produce Cerenkov photons that are transported through the column of water. A photon tally counts the photons crossing the plane at $z = 200$ cm. The tally used only counts photons with energies in the visible range travelling in a direction that is within a $\mu = 0.99995$ cone of the $+z$ direction. The pseudo-arbitrary angle restriction was originally added to screen out photons that have come from regions of the core other than the coolant channel of interest and to mimic the way a real photon detector such as a camera would be able to distinguish where the light is coming from using lenses and small apertures. In the water column model used for correlation factor generation, nearly all of the photons that make it to the tallying plane are within the angle bin, because those that are not will leave the column and enter a region of zero importance to die before ever reaching $z = 200$ cm. The results of this tally provide an estimate of the visible Cerenkov flux, which is then divided by the result of electron flux tally to get the correlation for the Cerenkov flux produced per unit of electron flux in the spatial and energy bin used in the model. The calculation of this response function for a single spatial bin “m” and energy bin “n” can be seen in Eq. (17),

$$\Sigma_{\text{Response}}(z_m, E_n) = \frac{\Psi_{\text{visible}}(200\text{cm}, \mathbf{s})}{\Phi_{\text{Electron}}(z_m, E_n)}, \quad (17)$$

where $\Psi_{\text{visible}}(200\text{cm}, \mathbf{s})$ is the photon flux detected at the tally at $z = 200$ cm with direction in a $\mu = 0.99995$ cone about \mathbf{s} , and $\Phi_{\text{Electron}}(z_m, E_n)$ is the electron flux within the designated bin. This is the reverse form of Eq. (15), and it allows for a single correlation factor of the response function to be calculated by tallying the visible photon flux above the core. Note that in these models for generating the correlation factors, $\Phi_{\text{Electron}}(z_m, E_n)$ also contains all electrons present, because any electrons with energies or positions outside of the bin are killed.

This process is done for all 368 combinations of energy ranges and spatial segments in the coolant channel to get what acts as a spatial and energy dependent response function for electrons in the coolant producing an observable Cerenkov response 2 m above the core. A table containing the ratio of the photon flux above the core to the electron flux within a segment and the corresponding Monte Carlo uncertainty for each of the 368 spatial and energy bins can be seen in Appendix A. The response function is essentially a

2D matrix that converts the electron flux in one region and energy group into a Cerenkov flux contribution above the core.

5. Response function verification

The response function relating the electron and photon fluxes can then be used to estimate the Cerenkov flux without requiring the actual production and tracking of Cerenkov photons. To verify this, the model consisting of only 4 pins in an infinite lattice, shown in Fig. 3 and Fig. 4 is used. In the course of this and other research efforts, it was found that MCNP6.1.1 has some issues where visible photons will travel almost unimpeded through what should be opaque materials such as steel or fuel. This issue is likely occurring in part because the low energy ($<1\text{keV}$) cross section data for photons and electrons in MCNP 6.11 and 6.2 only cover zero temperature targets, so molecular effects are not yet included (Werner, 2017). This behavior is not physically accurate, so a work around was developed. To avoid transporting visible photons through opaque materials, the following method involving two versions of the model was used.

The first version of the model is run using a kcode criticality source with neutrons, electrons and photons tracked, but no photons below the standard 100 keV cutoff and no Cerenkov production. This model uses a surface source write (SSW) card that records all of the gammas and electrons passing out of the cladding and into the coolant. The sole purpose of the first run is to produce the SSW file. The second model is run with the same geometry, with a 1 eV photon cutoff, with Cerenkov production enabled and with zero photon importance in all materials except the coolant to simulate opacity. This second model uses a surface source read (SSR) card to take the gammas and electrons leaving the pins and transport them through the coolant to produce electrons and Cerenkov photons. A visual comparison between the two models can be seen in Fig. 6.

The SSR model tallies the electrons in the 1 cm cylinder comprising most of the coolant channel with spatial and energy bins corresponding to the correlations previously calculated. The electron tally results for each spatial and energy bin are then multiplied by the correlation factor for that bin to obtain its contribution to the Cerenkov flux above the reactor. The contributions from all of the bins are added together as shown in Eq. (15) to estimate the total Cerenkov observed above the core. The resulting

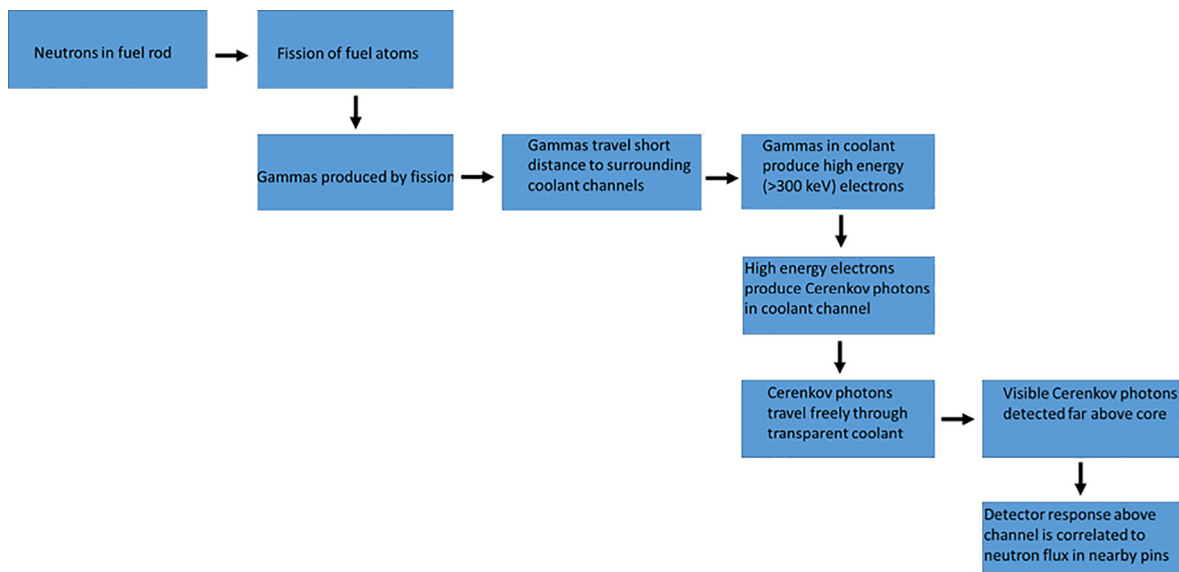


Fig. 3. Progression from neutrons in the fuel to Cerenkov detection above core.

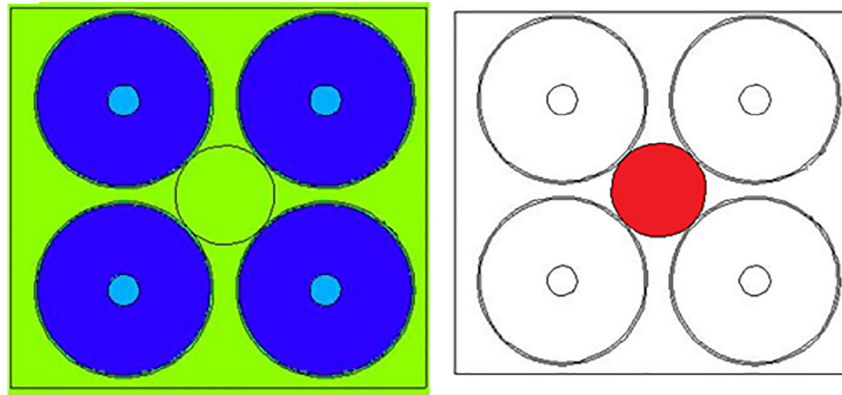


Fig. 4. XY cross sections of 4 pin model showing pins, coolant and the reflecting boundaries. (Right) the red region is the portion of the channel containing the electron tallies. (For interpretation of the references to colour in this figure legend, the reader is referred to the web version of this article.)

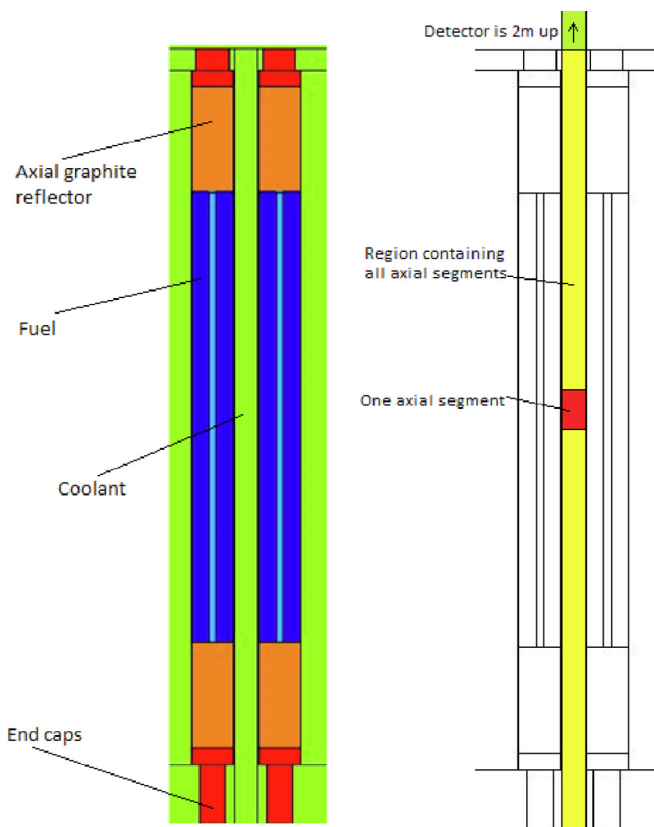


Fig. 5. Diagonal X/Y vs Z cross section showing 2 of the pins and the cylindrical region of the channel being tallied. (Left) color corresponds to materials so that the coolant and fuel pins can be seen. (Right) the red region corresponds to one axial segment being tallied, while the yellow region contains the other 15 axial segments tallied in separate MCNP runs. The green region shows the bottom of the column of water above the channel where the Cerenkov detection plane is located, 2 m above the core's axial centerline. (For interpretation of the references to colour in this figure legend, the reader is referred to the web version of this article.)

estimate of the Cerenkov flux at 200 cm above the core midplane is $5.46\text{E-}6$, normalized to the number of source neutrons from the SSW model. To verify the consistency of this method, the SSR model also tallies the Cerenkov photons crossing a plane at $z = 200$ cm within the 1 cm circle with directions in the $\mu = 0.9995$ cone. The Cerenkov flux from the direct tally is $5.919\text{E-}6$ per source particle. The ratio of the Cerenkov flux derived from the electron tally and response function based estimate to the

Cerenkov flux from the direct photon tally is 0.92. A small portion of the data involved in this estimate can be seen in Table 1, along with the summed total results and the direct tally results. The full data set, containing all 368 bins of the response function, as well as the electron flux and corresponding contribution to the Cerenkov flux above the core is in the attached data.

The ratio of 0.92 means that 92% of the observed photons tallied above the core were accounted for in the electron tally in the coolant channel. The less than 100% result is expected, because the regions outside of the cylindrical electron tally also contribute some to the flux directly above the channel. The 92% estimate result is considered sufficient verification that the Cerenkov response function based method developed here is internally consistent with MCNP's Cerenkov tracking model for finding the Cerenkov flux at the plane of interest above the core. One source of error that is not accounted for in that any reflection of light off the cladding is lost due to the killing of particles in the opaque regions; however, it is expected that this error is small because most of the photons that would have undergone reflection would have had directions outside the narrow cone about the vertical.

6. Cerenkov contribution to channel vs pin distance

To demonstrate the strength of the correlation between the Cerenkov flux above a channel and the fission density in nearby pins, a model of the full TRIGA core is run showing the contribution to the Cerenkov detectable above the core coming from a single fuel pin. This is done by only transporting gammas that were produced from fissions in one pin. To produce this model, an SSW and SSR run are performed. The SSW input deck runs with neutrons and gammas, with the core in its normal critical configuration. The gammas crossing the outer boundary of the cladding on the third pin of the third row of pins are recorded in the WSSA/RSSA file by the SSW card. The photon importance of all regions outside of this pin was set to zero, to ensure that gammas in other pins do not get included in the surface source. Then, the SSR model was run tracking photons and electrons to tally the energy and spatially dependent electron flux resulting from the gammas and electrons leaving the pin, such that the response function can be used to obtain the Cerenkov flux above each coolant channel at 2 m above the core midplane. The Cerenkov contribution to each of the 81 channels monitored for Cerenkov in the reactor can be seen in Fig. 7, with a black overlay of the reactor geometry. Plots using both a linear and logarithmic scale are shown.

This data was then used to produce a rough estimate of what the Cerenkov contribution to any channel from any pin is, based upon the distance between the pin and channel. The four channels

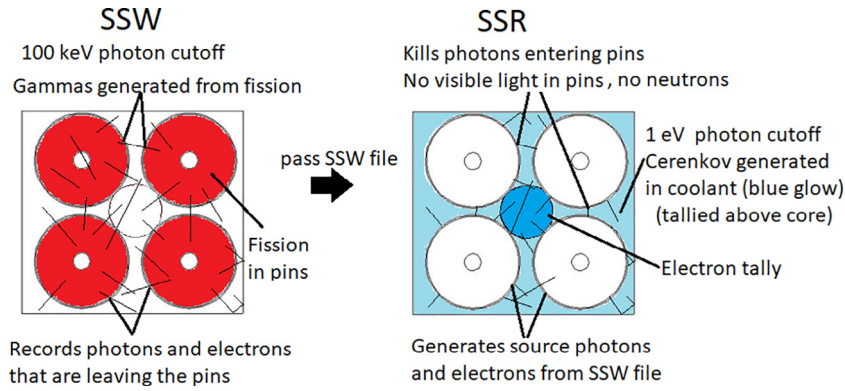


Fig. 6. Graphical comparison between SSW and SSR runs, with small lines denoting example gamma paths. The fission and gamma source from neutrons is shown in red in the SSW case. The SSR case represents the area producing Cerenkov radiation in blue, with the electron tally in the darker blue region. (For interpretation of the references to colour in this figure legend, the reader is referred to the web version of this article.)

Table 1

Example containing some of the data used to verify response functions and test what portion of the Cerenkov flux above the core the response function method captures.

segment number	Maximum bound of energy bin (MeV)	Pflux/Eflux response correlation factor	Electron flux from channel	Contribution to visible photon flux above channel
1	0.3	1.56E-04	1.46E-06	2.28E-10
1	0.4	1.32E-03	1.28E-06	1.69E-09
1	0.5	2.53E-03	1.13E-06	2.86E-09
1	0.6	2.86E-03	9.70E-07	2.77E-09
1	0.7	3.19E-03	8.42E-07	2.68E-09
1	0.8	3.43E-03	7.53E-07	2.58E-09
...
9	1.1	5.05E-03	6.19E-06	3.13E-08
9	1.2	5.24E-03	5.50E-06	2.88E-08
9	1.3	5.50E-03	4.84E-06	2.66E-08
9	1.4	5.21E-03	4.23E-06	2.21E-08
9	1.5	5.39E-03	3.73E-06	2.01E-08
9	1.6	5.46E-03	3.15E-06	1.72E-08
...
16	3.0	7.61E-03	2.42E-06	1.84E-08
16	4.0	7.16E-03	1.22E-06	8.76E-09
16	5.0	7.21E-03	8.12E-07	5.85E-09
16	10.0	7.54E-03	8.85E-07	6.67E-09
Sum of all visible photon flux contributions gives total estimated flux:				Sum = 5.4595E-06
Estimated photon flux from response function		Visible photon flux measured by tally at z = 2 m	Ratio of estimate from electron flux divided by tallied Cerenkov	
5.4595E-06		5.919E-06	0.92	

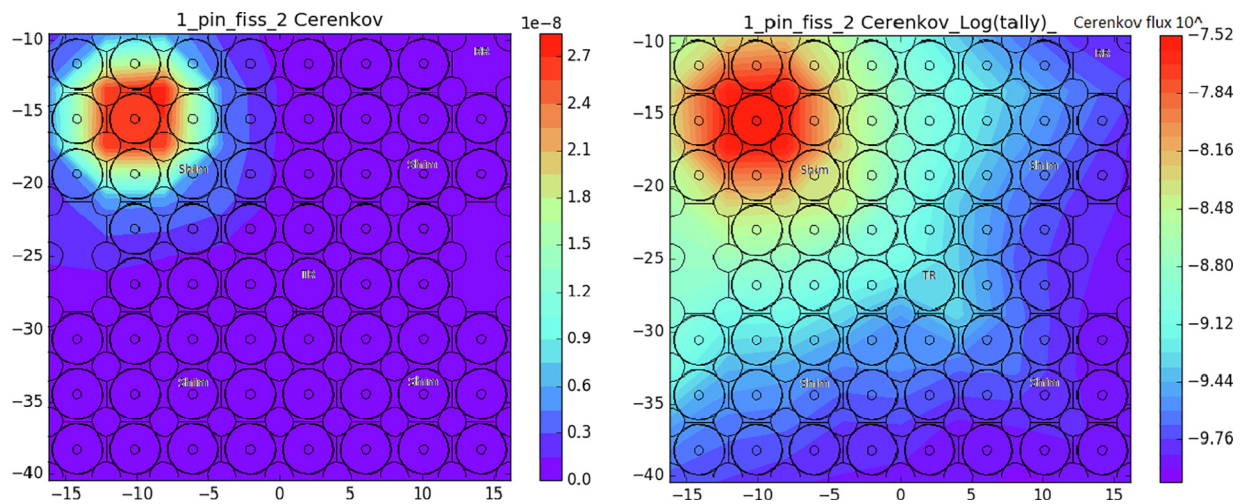


Fig. 7. Cerenkov flux above the core caused by a single fuel pin, calculated using electron tallies in the coolant channels and the response function. The plot on the left has a linear scale and the right has a log scale for the Cerenkov flux.

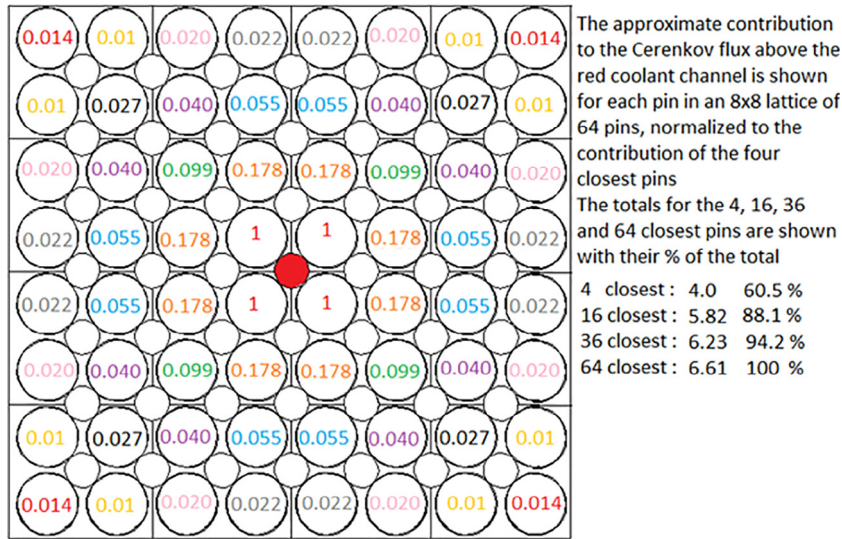


Fig. 8. Approximate contribution of every pin in an 8×8 grid to the Cerenkov flux above the central coolant channel, normalized to four closest pins. Approximation is based upon heterogeneous model of TRIGA core.

closest to the pin, at distance (0,0), are used as a normalization factor, meaning that the average Cerenkov flux in the four channels closest to the pin is used to divide all other contributions such that for the closest pins, the relative contribution is 1. The relative contribution of every other channel to pin distance up to three and a half pin pitch lengths of displacement in both the x and y direction, distance (3,3), was calculated as the average contribution of the pin to channels at that distance in the model divided by the average of the closest 4. For example, there are eight channels at a distance of (0,1) in the model, the 2 channels above the pin above the source pin, the 2 channels to the left of the pin to the left of the source, etc. So the average relative contribution for a channel to pin distance of (0,1) is given by Eq. (18):

$$\text{Relative contribution} = \frac{[\sum_{i=1}^8 \text{Cerenkov flux for channel } i \text{ at distance } (0,1)]/8}{[\sum_{j=1}^4 \text{Cerenkov flux for channel } j \text{ at distance } (0,0)]/4} = 0.178. \quad (18)$$

The contribution for a greater channel distance, such as (2,3) is limited by the fact that only 2 of the 8 possible channels at that distance are measured, thus the average of those two data points must be used, giving a relative contribution of 0.01. Variable shielding effects caused by the presence of the safety shim down and to the right of the gamma producing pin and the water holes also introduce some error. The furthest contribution considered is for the distance (3,3); however, there is only one channel in the reactor at that distance from the pin producing gammas and it is on the other side of the transient rod hole. Using this one point for the average actually causes it to have a larger relative contribution of 0.014 when compared to the (2,3) channel distance.

This information about the relative contribution of channels at an arbitrary displacement can be used similarly to an adjoint calculation in that the contribution of this one pin to any channel at a given displacement relative to the closest channel is the same as the contribution to a single channel for any pin at that displacement relative to the closest 4 pins to the channel. A symmetrical lattice approximation containing only fuel pins is then used to allow the relative channel contributions to cover an 8×8 grid of pins around a single coolant channel. As there are only 76 fuel pins in the TRIGA core, this 8×8 grid of 64 pins was deemed sufficient for the purpose of approximation, and the potential contribution of

anything further away is ignored. The total contribution of the 4, 16, 36 and 64 closest pins are also calculated by summation. The results of these calculations for relative contributions can be seen in Fig. 8.

This shows the four closest pins to a channel in a symmetric lattice contributing 60.5% of the total Cerenkov above the channel. Expanding to a 4×4 grid around the channel consisting of the 16 closest pins increases this to 88.1%. The other 11.9% of the Cerenkov light above the channel comes from pins further away than this.

A source of error in this approximation is that it uses a symmetric lattice of fuel pins, when the actual TRIGA core has many pin locations that are replaced by control rods, water spaces or experimental irradiation locations. The estimation of the contribution based upon distance also has error in that it is based upon a model of the actual TRIGA where some of the lattice locations do not contain fuel pins. Most notably, the estimates for the outermost corners in Fig. 8 higher than the next closest pins, because the only channel in the MCNP run that is 3.5 pin pitches away in both the x and y direction is directly across from the transient rod. As seen in Fig. 7, this location actually has a slightly higher Cerenkov flux estimate than its nearer neighbor at a displacement of $3.5 \times$ and $2.5 y$, because the transient rod location contains a gas that doesn't provide as much gamma shielding. Another error source is that this assumes each pin has a constant power, when in the actual core, the more central pins will have a higher power and thus contribute slightly more to a given channel. Finding highly accurate correlations between the fission density in each pin and each coolant channel would require separate models for each segment of each of the 74 pins, which is outside of the scope of this research effort.

7. Conclusion

The response function for relating the electron flux in a channel to Cerenkov flux above the channel in (Hearne, 2020) was successfully generated and verified for internal consistency within MCNP. It was found that the response function and electron tallies accounted for 92% of the Cerenkov photons produced by the four surrounding pins. In a large symmetric 8×8 lattice of 64 pins, the four closest pins to a coolant channel contribute 60.5% of the total Cerenkov above the core, while the 16 closest pins in a

4×4 grid around the channel account for 88.1% of the total, with the rest coming from pins that are further away. A large portion of the Cerenkov above a channel comes from nearby pins, so a Cerenkov light detector above a channel is usable for estimating the local power density of the pins near that channel.

Declaration of Competing Interest

The authors declare that they have no known competing financial interests or personal relationships that could have appeared to influence the work reported in this paper.

Acknowledgements

This research is being performed using funding received from the DOE Office of Nuclear Energy's Nuclear Energy University Program, NEUP Award Number DE-NE0008306.

Disclaimer

This paper was prepared as an account of work sponsored by an agency of the United States Government. Neither the United States Government nor any agency thereof, nor any of their employees, makes any warranty, expressed or implied, or assumes any legal

liability or responsibility for the accuracy, completeness, or usefulness of any information disclosed.

Any views, opinions, findings, conclusions, or recommendations expressed in this publication are those of the authors and do not necessarily state or reflect the views of the Department of Energy Office of Nuclear Energy.

References

- Berger, M., Coursey, J., Zucker, M., Chang, J., July 2017. Stopping-Power & Range Tables for Electrons, Protons, and Helium Ions (ESTAR), NIST Standard Reference Database 124.
- Durkee, J.W., James, M.R. 2013-07-17. MCNP6 Cerenkov Radiation Feature Verification, Los Alamos National Lab, Los Alamos, New Mexico.
- Goorley, T., 2014. "MCNP6.1.1-Beta Release Notes," Los Alamos National Lab.
- Hearne, J.A., Tsvetkov, P.V., 2020. Spatial power profiling method using visual information in reactors with optically transparent coolants. *Ann. Nucl. Energy.* 137, 107071. <https://doi.org/10.1016/j.anucene.2019.107071>.
- Horvath, A., 2006. Artist, The geometry of the Cerenkov radiation (shown for the ideal case of no dispersion). [Art].
- Litjens, R.A.J., Quickenden, T.I., Freeman, C.G., 1999. Visible and near-ultraviolet absorption spectrum of liquid water. *Appl. Opt.* 38 (7), 1216–1223.
- Morel, A., 1974. Optical properties of pure water and pure sea water. In: *Optical Aspects of Oceanography*, New York, Academic Press, pp. 1–24.
- Quickenden, T.I., Irving, J.A., 1980. The ultraviolet absorption spectrum of liquid water. *J. Chem. Phys.* 72, 4416.
- Wang, L.V., Wu, H.L., 2007. *Biomedical Optics*. Wiley.
- Werner, C.J. 2017. MCNP Users Manual – Code Version 6.2.